03 Jun 2022

Synthesis, Physicochemical Characterization, and Catalytic Evaluation of Fe^{3+}-Containing SSZ-70 Zeolite

Christopher M. Lew

Cong Yan Chen

Gary J. Long
Missouri University of Science and Technology, glong@mst.edu

Fernande Grandjean
Missouri University of Science and Technology, grandjeanf@mst.edu

et. al. For a complete list of authors, see https://scholarsmine.mst.edu/chem_facwork/3191

Recommended Citation

C. M. Lew and C. Y. Chen and G. J. Long and F. Grandjean and A. S. Ichimura and D. Xie and N. A. Grosso-Giordano and K. Chakarawet and H. S. Lacheen and K. O. Jensen and A. Martinez and A. Katz and B. Z. Zhan and S. I. Zones, "Synthesis, Physicochemical Characterization, and Catalytic Evaluation of Fe^{3+}-Containing SSZ-70 Zeolite," *ACS Catalysis*, vol. 12, no. 11, pp. 6464 - 6477, American Chemical Society, Jun 2022.
The definitive version is available at https://doi.org/10.1021/acscatal.2c01361

ACS Catalysis

pubs.acs.org/acscatalysis Research Article

Synthesis, Physicochemical Characterization, and Catalytic Evaluation of Fe^{3+}-Containing SSZ-70 Zeolite

Christopher M. Lew,* Cong-Yan Chen, Gary J. Long, Fernande Grandjean, Andrew S. Ichimura, Dan Xie, Nicolás A. Grosso-Giordano, Khetpakorn Chakarawet, Howard S. Lacheen, Kurt O. Jensen, Abraham Martinez, Alexander Katz, Bi-Zeng Zhan, and Stacey I. Zones

Cite This: *ACS Catal.* 2022, 12, 6464−6477 Read Online

ACCESS | Metrics & More | Article Recommendations | Supporting Information

ABSTRACT: Whereas one-dimensional, 10-membered ring zeolites are typically used for hydroisomerization, Fe^{3+}-containing SSZ-70 (Fe-SSZ-70) shows remarkable isomerization selectivity for a zeolite containing 12- and partially blocked 14-membered rings, in addition to 10-membered rings. Fe-SSZ-70 was compared to Al^{3+}-containing SSZ-70 (Al-SSZ-70) in constraint index and *n*-decane hydrocracking tests. Fe-SSZ-70 exhibited a 74% total isomer yield (64% yield of monobranched isomers and 10% cracking yield) at 85% conversion compared to 49% total isomer yield (41% yield of monobranched isomers and 36% cracking yield) for Al-SSZ-70 at the same conversion. The selectivity to isomerization is attributed to the weaker acid strength of Fe-SSZ-70 over Al-SSZ-70. Fe-SSZ-70 was directly synthesized with Fe^{3+} isomorphously substituted in tetrahedral positions. The coordination environment of the Fe^{3+} was characterized using Mössbauer, electron paramagnetic resonance, and diffuse reflectance UV−vis spectroscopies. The physicochemical properties were further probed with inductively coupled plasma atomic emission spectroscopy, temperature-programmed desorption of isopropylamine, and nitrogen adsorption−desorption. The Fe^{3+} was tetrahedrally coordinated in the as-made materials and became partially octahedrally coordinated upon calcination; enough Fe^{3+} remained in the framework after calcination for Fe-SSZ-70 to remain catalytically active.

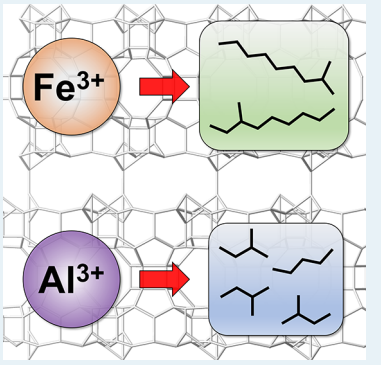

KEYWORDS: *ferrosilicate zeolite, SSZ-70, cracking, hydrocracking, hydroisomerization*

1. INTRODUCTION

The properties of fuels and base oils are generally enhanced when linear alkanes are branched. For fuels, this results in a higher octane number and better low-temperature performance; monobranching in base oils leads to better pour and freezing points. Monobranched isomers are formed first in the hydroisomerization of linear alkanes, followed by multibranched products and then cracked products.[1] The zeolites that are used for the isomerization of linear alkanes traditionally have one-dimensional, 10-membered ring channels (1D, 10-MR).[2−4] Isomerization occurs at the mouth of the pore channel,[5] and the branched products diffuse away from the zeolite because the size of the 10-MR channels selectively restricts diffusion of the branched isomers into the channels. On the other hand, 12-MR zeolites are able to host isomerized products that can further branch and crack at the acid sites in the pores.[6] 1D channels help reduce coke formation and increase catalyst lifetime. Thus, the shape selectivity of 1D, 10-MR zeolites is thought to be ideal. While numerous studies have tested both multidimensional and 12-MR Al^{3+}-containing zeolites, none have an isomer selectivity as high as 1D, 10-MR zeolites to the best of our knowledge.

SSZ-70 is synthesized as a layered precursor material with **MWW**-type layers.[7−9] (The International Zeolite Association assigned SSZ-70 the three-letter framework code ***-SVY**; * indicates a disordered material and - indicates an interrupted framework in which not all T-atoms are four-connected.) The structure of calcined Si-SSZ-70 was recently solved using a combination of synchrotron X-ray powder diffraction, two-dimensional dynamic nuclear polarization-enhanced magic angle spinning nuclear magnetic resonance spectroscopy, and high-resolution transmission electron microscopy.[7] Although the layers of SSZ-70 are related to ones found in the **MWW** family of zeolites, they are arranged differently, which endows the SSZ-70 material with several distinct differences from other members of the **MWW** family. During the calcination of MCM-22(P), which is the layered precursor to the **MWW**-type material MCM-22 (MCM-22 and SSZ-25[10] are isostructural to one another), six silanol groups from the surface of one layer condense directly upon another six silanol groups from the

Received: March 20, 2022
Revised: May 3, 2022
Published: May 16, 2022

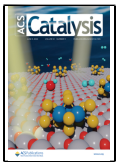

https://doi.org/10.1021/acscatal.2c01361
ACS Catal. 2022, 12, 6464−6477

adjacent layer to form a 12-MR **MWW** cage in the interlayer region.[11] However, the layers in the precursor to SSZ-70 are disordered and shifted by ±1/3 of a unit cell along the ⟨110⟩ direction.[7] As a result, only half as many silanols condense, and the interlayer region in SSZ-70 forms a 14-MR that is partially blocked by silanol groups, which differs from the 10-MR channel system formed in calcined **MWW**. The resulting silanol groups exist as a single isolated silanol group and a separate nest of three silanol groups in the interlayer regions.[12] SSZ-70 retains the **MWW**-type 12-MR side pockets on the surface of the **MWW** layer, as well as the 10-MR channels within the **MWW** layers. The stacking sequence is nearly random, although some ABAB stacking is observed.

The layered precursors of zeolites, including **MWW**-type zeolites,[13] **FER**,[14] **CDO**,[15,16] and others, can be modified using post-synthetic treatments to create new zeolitic materials with three-dimensional and/or hierarchical nanoarchitectures. For example, MCM-22(P) is the precursor of **MWW**, and it can be (1) calcined to create the three-dimensional zeolite **MWW**, (2) delaminated to form individual two-dimensional **MWW** sheets, and (3) swollen and pillared to produce MCM-36, which contains both zeolitic micropores and larger mesopores.[13] The synthesis of the all-silica, aluminosilicate, and borosilicate forms of SSZ-70 has been previously described,[17−19] and these materials have similarly been post-synthetically modified to create delaminated and hierarchical structures.[20,21] The delaminated materials, which possess higher surface areas than their three-dimensional counterparts, have shown higher activity in aromatic alkylation,[22] olefin epoxidation,[23] and Baeyer−Villiger oxidation.[24] Al^{3+}-containing SSZ-70, herein referred to as Al-SSZ-70, that was pillared showed increased activity for benzylation of mesitylene as compared to directly calcined Al-SSZ-70.[21] Directly calcined Al-SSZ-70 shows promise as a catalyst for olefin oligomerization.[25]

We used delaminated Al-SSZ-70 in vacuum gas oil hydrocracking tests for distillate production, and Figure 1 shows the relative product yields of delaminated Al-SSZ-70 against a commercial hydrocracking catalyst. The results are presented based on the simulated distillation (non-loss Simdist).[26] The target distillate product had a boiling range of 121−260 °C, of which the commercial hydrocracking catalyst had higher yields than Al-SSZ-70. On the other hand, Al-SSZ-70 had higher yields in the lower boiling range products, C_5−121 °C and C_4− (where C_5 refers to hydrocarbon chains with five carbons and C_4− refers to hydrocarbon chains with four or fewer carbons). These results indicate that Al-SSZ-70 overcracks when targeting for the 121−260 °C distillate product and suggest that the acid sites are too strong for this application. In contrast, the acid sites in B^{3+}-containing SSZ-70 (B-SSZ-70) are too weak to be useful under the same conditions (data not shown).

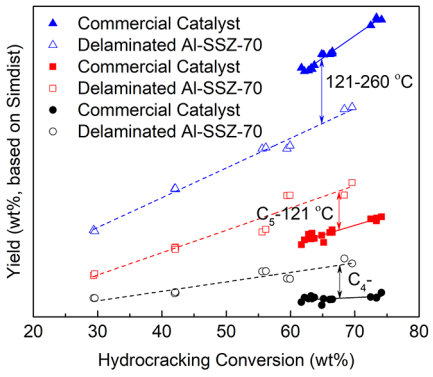

Figure 1. Yields of three different boiling range products versus the conversion of a vacuum gas oil feed in hydrocracking for delaminated Al-SSZ-70 and a commercial hydrocracking catalyst. The yields are based on simulated distillation.[26] The vertical arrows indicate the pair of the commercial hydrocracking catalyst and delaminated Al-SSZ-70 yields to compare at each cut point.

Isomorphic substitution of Fe^{3+} into the tetrahedral positions of other zeolite frameworks has shown that Fe^{3+} has an intermediate acid strength to that of aluminum and boron. By using both density functional theory (DFT) and methanol dehydration experiments on **MFI** zeolite, Jones et al. found that the heteroatom composition controls the strength of the acid site.[27] Earlier experimental work by Chu and Chang used ammonia temperature-programmed desorption (TPD) to study **MFI** materials substituted with various heteroatoms and found that Brønsted acid site strength increased according to Si < B < Fe < Ga < Al.[28] Numerous other DFT studies have reached similar conclusions.[29−32]

To determine whether a heteroatom with intermediate acidity could help reduce overcracking, Fe^{3+}-containing SSZ-70 (Fe-SSZ-70) was prepared through a direct synthesis method.[33] The synthesis of Fe^{3+}-substituted MCM-22 has been previously published[34] and Fe^{3+} has also been post-synthetically grafted onto delaminated SSZ-70.[35] This report, however, describes the first experimental example of the direct synthesis of SSZ-70 with the isomorphic substitution of Fe^{3+}. 1,3-Dicyclohexylimidazolium hydroxide (DCHI) and 1,3-diisobutylimidazolium hydroxide (DIBI) were used as organic structure-directing agents (OSDAs; Figure 2) under a wide range of Si/Fe atomic ratios, and both hydroxide and fluoride conditions can produce Fe-SSZ-70. The physicochemical properties of Fe-SSZ-70 were characterized, and several methods were employed to probe the coordination environment of Fe^{3+}. Fe-SSZ-70 was tested for the hydrocracking of *n*-decane, and its cracking and isomerization performance was compared to that of Al-SSZ-70.

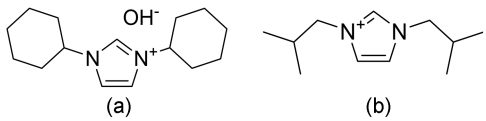

Figure 2. Chemical structures of (a) 1,3-dicyclohexylimidazolium hydroxide and (b) 1,3-diisobutylimidazolium hydroxide.

2. EXPERIMENTAL SECTION

2.1. Synthesis of Fe-SSZ-70 Using DCHI under Hydroxide Conditions. Synthesis conditions are listed in Table 1. The optimal synthesis conditions are described in detail here, which represent Example 9 in Table 1. Water (1.56 g), 0.16 g of sodium hydroxide (50 wt % solution), and 9.70 g of DCHI (10 wt % solution) were added to a 23 mL Teflon liner. The solution was stirred until homogeneous. Cabosil M5 (1.20 g) was slowly added and stirred until the solution was homogeneous. Iron(III) nitrate nonahydrate (0.16 g) was added. The final molar composition of the synthesis gel was 1 SiO_2/0.01 Fe_2O_3/0.05 Na_2O/0.2 DCHI/30 H_2O. The Teflon liner was transferred to an autoclave and heated in a 150 °C

https://doi.org/10.1021/acscatal.2c01361
ACS Catal. 2022, 12, 6464−6477

Table 1. Synthetic Conditions[a] and X-ray Diffraction (XRD) Results for Samples Made in Hydroxide Media Using DCHI as the OSDA

	molar ratio			
example	Si/Fe	Na/Si	H_2O/Si	XRD results
1	15	0.200	30	amorphous
2	15	0.250	30	amorphous
3	25	0.150	30	SSZ-70
4	25	0.200	30	SSZ-70
5	33	0.105	30	SSZ-70
6	42	0.102	30	SSZ-70
7	50	0.100	20	SSZ-70
8	50	0.100	26	SSZ-70
9	50	0.100	30	SSZ-70
10	50	0.100	35	SSZ-70
11	50	0.100	40	SSZ-70
12	100	0.095	30	SSZ-70
13	250	0.092	30	SSZ-70

[a]Synthesis was carried out over 7 days at 150 °C at a DCHI/Si molar ratio of 0.2.

oven with rotation at 43 rpm for 7 days. The product was filtered and washed with deionized water.

2.2. Synthesis of Fe-SSZ-70 Using DIBI under Hydroxide Conditions. Synthesis conditions are listed in Table 2. The optimal synthesis conditions are described in detail here, which represent Example 17 in Table 2. Sodium hydroxide (0.18 g, 50 wt % solution) and 9.96 g of DIBI (9 wt % solution) were added to a 23 mL Teflon liner. The solution was stirred until the solution was homogeneous. Cabosil M5 (1.40 g) was slowly added and stirred until the solution was homogeneous. Iron(III) nitrate nonahydrate (0.19 g) was added. Water (1.13 g) was evaporated from the solution by gently blowing a stream of nitrogen over the top of the solution. The final molar composition of the synthesis gel was 1 SiO_2/0.01 Fe_2O_3/0.05 Na_2O/0.2 DIBI/20 H_2O. The Teflon liner was then transferred to an autoclave and heated in a 150 °C oven with rotation at 43 rpm for 7 days. The product was filtered and washed with deionized water.

Table 2. Synthetic Conditions[a] and XRD Results for Samples Made in Hydroxide Media Using DIBI as the OSDA

		molar ratio			
example	time (days)	Si/Fe	Na/Si	H_2O/Si	XRD results
14	42	25	0.200	30	amorphous
15	42	33	0.105	30	amorphous
16	7	42	0.102	30	**MTW**
17	7	50	0.100	20	SSZ-70
18	7	50	0.100	25	**MTW**
19	7	50	0.100	30	**MTW**
20	7	50	0.100	35	**MTW**
21	12	50	0.100	50	**EUO**
22	22	100	0.095	30	SSZ-70
23	12	250	0.092	30	SSZ-70

[a]Synthesis was carried out at 150 °C at a DIBI/Si molar ratio of 0.2.

2.3. Synthesis of Fe-SSZ-70 under Fluoride Conditions. Synthesis conditions are listed in Table 3. The optimal synthesis conditions are described in detail here, which represent Example 26 in Table 3. Tetraethylorthosilicate (TEOS, 5.00 g) was added to 26.41 g of DIBI (9 wt % solution) in a polyethylene bottle. The TEOS was stirred and hydrolyzed overnight. The resulting ethanol and 21.35 g of water were evaporated by gently blowing a stream of nitrogen over the top of the solution. Then, 0.50 g of hydrofluoric acid (48%) was added and the mixture was homogenized with a spatula. Iron(III) nitrate nonahydrate (0.20 g) was added, and the mixture was homogenized with a spatula. The final molar composition of the synthesis gel was 1 SiO_2/0.01 Fe_2O_3/0.5 HF/0.5 DIBI/5 H_2O. The contents of the polyethylene bottle were transferred to a Teflon liner and heated in a 150 °C oven under static conditions for 19 days. The product was filtered and washed with deionized water.

Table 3. Synthetic Conditions[a] and XRD Results for Samples Made in Fluoride Media Using DCHI and DIBI as the OSDAs

		molar ratio		
example	time (days)	OSDA	H_2O/Si	XRD Results
24	14	DCHI	5	SSZ-70 + unknown
25	14	DCHI	10	amorphous
26	19	DIBI	5	SSZ-70
27	28	DIBI	10	amorphous

[a]Synthesis was carried out at 150 °C at molar ratios of Si/Fe = 50, OSDA/Si = 0.5, and HF/Si = 0.5.

2.4. Synthesis of Al-SSZ-70 Using DCHI under Hydroxide Conditions (Example 28). Al-SSZ-70 was synthesized as a reference for this study on Fe-SSZ-70 materials. The details of its synthesis are as follows: 1.61 g of water, 0.16 g of sodium hydroxide (50 wt % solution), and 9.70 g of DCHI (10 wt % solution) were added to a 23 mL Teflon liner. The solution was stirred until homogeneous. Reheis F-2000 aluminum hydroxide (0.04 g) was added, and the mixture was stirred until homogeneous. Then, 1.20 g of Cabosil M5 was slowly added and stirred until the solution was homogeneous. The final molar composition of the synthesis gel was 1 SiO_2/0.01 Al_2O_3/0.05 Na_2O/0.2 DCHI/30 H_2O. The Teflon liner was transferred to an autoclave and heated in a 160 °C oven with rotation at 43 rpm for 7 days. The product was filtered and washed with deionized water.

2.5. Calcination. The as-made zeolite was spread into a thin layer on a calcination dish and heated in a muffle furnace in flowing air to 120 °C at a rate of 1 °C/min and held at 120 °C for 2 h. The temperature was then increased at 1 °C/min to 550 °C and held at 550 °C for 5 h.

2.6. Ammonium Exchange. The calcined material was ion-exchanged into the ammonium form by adding it to a 10 wt % ammonium nitrate solution in a mass ratio of 10/1 for 10 wt % NH_4NO_3 solution to calcined SSZ-70. The solution was heated statically at 95 °C for at least 2 h. The solution was decanted, and the process was repeated two more times. Following the final exchange, the zeolite was washed with deionized water to a conductivity of less than 50 μS/cm and dried at 95 °C. The NH_4^+-form of SSZ-70 was converted to the H^+-form by using the same calcination procedure as above.

2.7. Physicochemical Characterization. XRD was measured on a Panalytical Empyrean instrument using Cu Kα radiation. Scanning electron microscopy (SEM) was performed on a JEOL JSM 6700 F instrument. Elemental analysis was measured using inductively coupled plasma atomic emission spectroscopy (ICP-AES) by Galbraith Laboratories, Inc. Nitrogen adsorption−desorption was performed on a

https://doi.org/10.1021/acscatal.2c01361
ACS Catal. 2022, 12, 6464−6477

Micromeritics ASAP 2010, and the micropore volume and external surface area were calculated using the *t*-plot method.[36] Temperature-programmed desorption (TPD) experiments using isopropylamine were measured on a TA Instruments Q5000 IR. The sample was pre-treated at 400 °C for 1 h in flowing N_2. The dehydrated sample was then cooled to 120 °C in flowing N_2 and held for 30 min in flowing N_2 saturated with isopropylamine. The sample was then heated to 500 °C at a rate of 10 °C/min in flowing N_2. Palladium dispersion was measured on a Quantachrome Autosorb iQ. The sample was pre-treated according to the procedure outlined in Table S1, at which point the total hydrogen chemisorption was measured at 110 °C at the following pressures: 24, 29, 35, 39, 44, 48, and 53 kPa. The sample was then placed under vacuum for 10 min, and the isothermal hydrogen chemisorption was repeated to determine the weak and strong hydrogen chemisorption components. The dispersion values were calculated and reported based on the actual Pd loading from ICP-AES analysis.

Zero-field iron-57 Mössbauer spectra were measured in a constant acceleration SEE Corp. spectrometer that utilized a room-temperature rhodium matrix cobalt-57 source. The zeolite absorber was placed in a nylon washer sealed with Kapton tape and studied in a Janis Research cryostat that was cooled with a helium-closed cycle refrigerator for the 5 K spectrum. The spectrometer was calibrated at 290 K with a 30 μm α-iron foil. All isomer shifts are reported relative to α-iron at 290 K. The thickness of the Mössbauer spectral absorbers was about 50 mg/cm^2 of the sample as a fine powder.[37]

Electron paramagnetic resonance (EPR) spectra were measured on a Varian E-12 spectrometer. The field sweep and signal average were controlled by the EWWin software and hardware package. 2,2-Diphenyl-1-picrylhydrazyl (g = 2.0037) was used to calibrate the magnetic field.

Diffuse reflectance UV−vis (DRUV−vis) spectroscopy was performed on a Varian Cary 4000 spectrophotometer fitted with a praying mantis attachment from Harrick Scientific Products. Compacted poly-(tetrafluoroethylene) powder was used as a standard perfect reflector for the baseline corrections. The spectra are reported using Kubelka−Munk pseudo-absorbance and normalized to the maximum value of absorbance.

2.8. Preparation of the Hydrocracking Catalyst. The ammonium form of SSZ-70 was ion-exchanged in an aqueous palladium nitrate solution at a pH of ∼10 for a Pd loading of 0.5 wt % (dry wt basis). The zeolite was washed with deionized water to a conductivity of less than 50 μS/cm and dried. The zeolite was then calcined in air at 482 °C for 3 h with a ramp rate of 1 °C/min.

2.9. Constraint Index (CI). H^+-form SSZ-70 (0.5 g) was pelletized at 5000 psi, meshed to 20−40, and charged into a 3/8 in stainless steel reactor with alundum on both sides of the zeolite bed. Helium was introduced into the reactor tube at a rate of 10 cm^3/min at atmospheric pressure. The reactor was heated in a Lindburg furnace to 454 or 482 °C, and a 50/50 (wt %/wt %) feed of n-hexane and 3-methylpentane was introduced into the reactor at a rate of 8 μL/min using a Brownlee pump. Direct sampling via on-line gas chromatography began 15 min after feed introduction.

2.10. Hydrocracking of *n*-Decane (nC$_{10}$). The Pd-loaded sample (0.5 g) was pelletized at 5000 psi, meshed in a 20−40 range, and charged into a 0.25 in outside diameter stainless steel reactor. Alundum was loaded upstream of the catalyst, and the reactor was pressurized to 1200 psig using hydrogen. The catalyst was reduced at 315 °C for 1 h in a hydrogen flow of 160 mL/min. The run conditions were as follows: a total pressure of 1200 psig; a down-flow hydrogen rate of 8.3 mL/min, when measured at 1 atmospheric pressure and 25 °C; and a down-flow *n*-decane liquid feed rate of 0.66 mL/h. Products were analyzed by on-line gas chromatography every 30 min. Conversion is defined as the amount of *n*-decane that reacted to produce other products, including isomers of C_{10}. Yields are expressed as mole percent of products other than *n*-decane and include the C_{10} isomers as a yield product.

nC$_{10}$ test is a standard test reaction at the Chevron Technical Center research facility. Reproducibility of the reactor and on-line GC analysis are frequently tested with a few standard catalysts (and occasionally some purposefully selected catalysts). In addition, at least five sequential on-line GC data points (each per 60 min) are acquired for each temperature reported in the nC$_{10}$ data to ensure reproducibility before moving on to the next reaction temperature in our continuous experiments. Furthermore, after going through the temperature profile, the reactor is then brought back to selected temperatures to check the reproducibility of the results and catalyst stability at these selected temperatures before and after having finished the entire temperature profile. The Pd/Fe-SSZ-70 and Pd/Al-SSZ-70 samples tested in this study did not show evidence of deactivation over the time scales of these reactions (3−7 days).

3. RESULTS

3.1. Synthesis. Tables 1 and 2 show synthesis conditions and XRD results for samples made in hydroxide media using DCHI and DIBI. Under these conditions, DCHI consistently produces as-made SSZ-70 materials from gels with a wide range of atomic Si/Fe molar ratios from 25 to 250. Conversely, DIBI also results in **MTW** and **EUO** phases, although SSZ-70 can still be made from gels with atomic Si/Fe ratios from 50 to 250. The appearance of 1D, 10-MR, and 12-MR phases is not surprising for DIBI: previous studies using this OSDA have also resulted in **MTW**,[19] and more generally, imidazolium-based OSDAs are known to produce 1D, 10-, and 12-MR zeolites.[38] For the gels made in this study with DIBI at a Si/Fe ratio of 50, the water content seems to be the controlling factor for phase selectivity (Table 2). As the water content increases and gel pH decreases, the resulting phases reduce in dimensionality and pore size from a multidimensional zeolite with both 10- and 12-MR (SSZ-70) to a 1D, 12-MR (**MTW**) to a 1D, 10-MR (**EUO**).

Table 3 shows synthesis conditions and XRD results for samples made in fluoride media using DCHI and DIBI. Both OSDAs are capable of making SSZ-70, although a pure-phase SSZ-70 was not attainable using DCHI. Similar results for Al-SSZ-70 in fluoride were previously found in which DIBI was more selective than DCHI over a Si/Al range from 15 to ∞: DIBI led to SSZ-70 over this range, whereas DCHI also resulted in a different phase (***BEA**).[19,39]

Note that subsequent physicochemical characterization and catalytic tests are reported for the hydroxide version of Fe-SSZ-70 using DCHI (Example 9 as described in the Experimental Section). The only exceptions are Figures S1 and S2, which show the XRD patterns of as-made Fe-SSZ-70 synthesized under hydroxide and fluoride conditions, respectively, using DIBI as the OSDA. These two samples correspond to Examples 17 and 26, respectively, from Tables 2 and 3.

https://doi.org/10.1021/acscatal.2c01361
ACS Catal. 2022, 12, 6464−6477

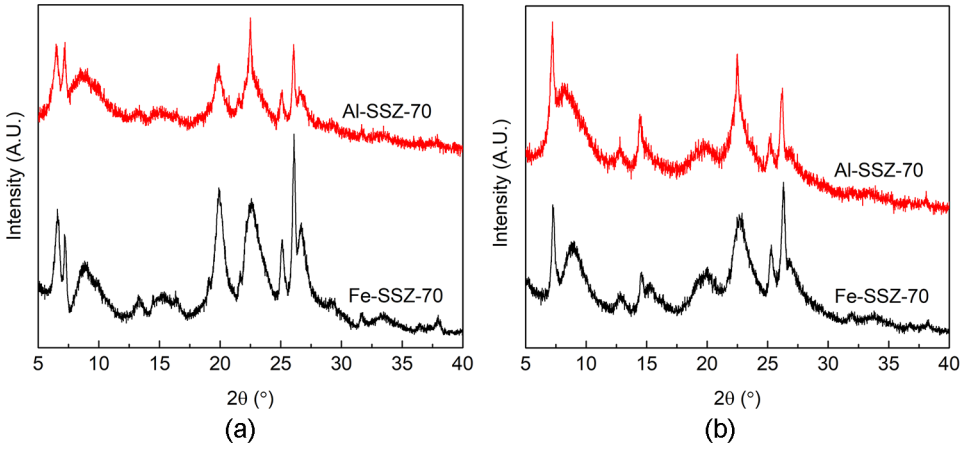

Figure 3. XRD patterns of (a) as-made Fe-SSZ-70 and Al-SSZ-70 and (b) calcined Fe-SSZ-70 and Al-SSZ-70. The Fe-SSZ-70 samples are Example 9, and the Al-SSZ-70 samples are Example 28.

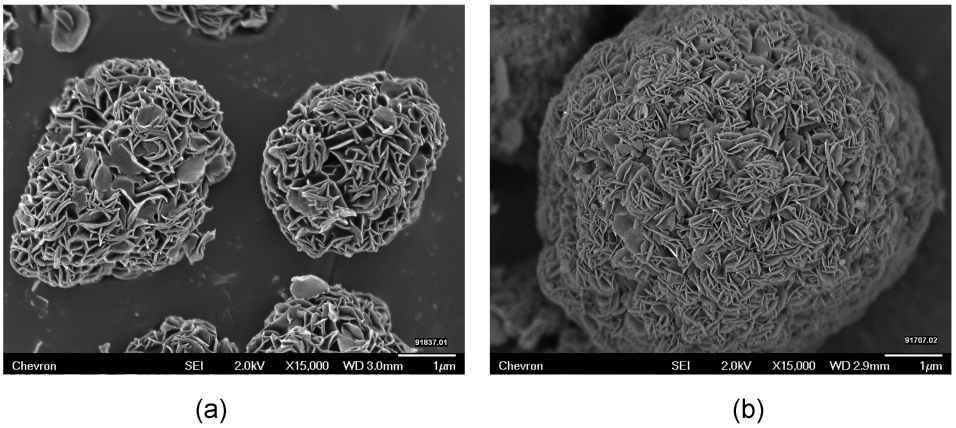

Figure 4. SEM images of (a) as-made Fe-SSZ-70 and (b) as-made Al-SSZ-70.

Table 4. Chemical and Textural Properties of As-Made and Calcined Fe-SSZ-70 and Al-SSZ-70 Samples

sample	Si/M_{gel} [a]	$Si/M_{product}$ [a]	theoretical acid site density (μmol/g) [b]	experimental acid site density (μmol/g) [c]	micropore volume (cm^3/g)	external surface area (m^2/g)
$Fe\text{-}SSZ\text{-}70_{as\text{-}made}$	50	44				
$Fe\text{-}SSZ\text{-}70_{calcined}$		46	354	180	0.17	103
$Al\text{-}SSZ\text{-}70_{as\text{-}made}$	50	40				
$Al\text{-}SSZ\text{-}70_{calcined}$		45	358	270	0.17	107

[a]M = Fe or Al; Si/M ratios are calculated from Si, Al, and Fe wt % measurements from ICP-AES. [b]Calculated from $Si/M_{product}$ ICP-AES values for the calcined samples by assuming one acid site per M^{3+} ion. [c]Measured by isopropylamine TPD.

3.2. X-ray Diffraction. Roth et al. performed an extensive XRD analysis on several members of the **MWW** family, including EMM-10(P), MCM-22(P), MCM-49, and MCM-56,[40] while other members of the **MWW** family have been classified in another paper by Grzybek et al.[41] Specifically, Roth et al. studied the 6−7.5° and 7.5−10° 2θ regions of the XRD patterns. The peaks in the 6−7.5° 2θ region consist of either a singlet or a doublet from the (002) and (100) reflections. A singlet represents a contracted stacking repeat (~25 Å), whereas a doublet results from an expanded interlayer separation in the *c*-axis (~27 Å). Similarly, the 2θ region between 7.5 and 10° consists of either two discrete peaks ((101) and (102) reflections) or one broad peak. Those materials with two peaks exhibit aligned stacking of the layers along the *c*-axis, while those with the broadband have layers that are twisted off-register (vertically misaligned).

Figure 3a shows the XRD patterns of the as-made forms of Fe- and Al-SSZ-70 (Examples 9 and 28 from the Experimental Section, respectively). These patterns are similar to those of the original patents and early publications on SSZ-70.[17−19,39] Both samples exhibit two reflections in the 6−7.5° 2θ region and a broader peak in the 7.5−10° 2θ region; in those two regions, the Fe- and Al-SSZ-70 patterns resemble that of EMM-10(P). However, the merged (101)/(102) peak in the Fe- and Al-SSZ-70 samples centered at 8.8° is much better defined than the broadband observed in EMM-10(P).[40] This better resolution indicates the ±1/3 shift of the layers in the ⟨110⟩ direction, which is one of the defining features of SSZ-70 versus the other members of the **MWW** family.[7]

After calcination (Figure 3b), the peak at 6.5° disappears in the Fe- and Al-SSZ-70 XRD patterns, indicating that the **MWW** layers condense together; these patterns resemble that

https://doi.org/10.1021/acscatal.2c01361
ACS Catal. 2022, 12, 6464−6477

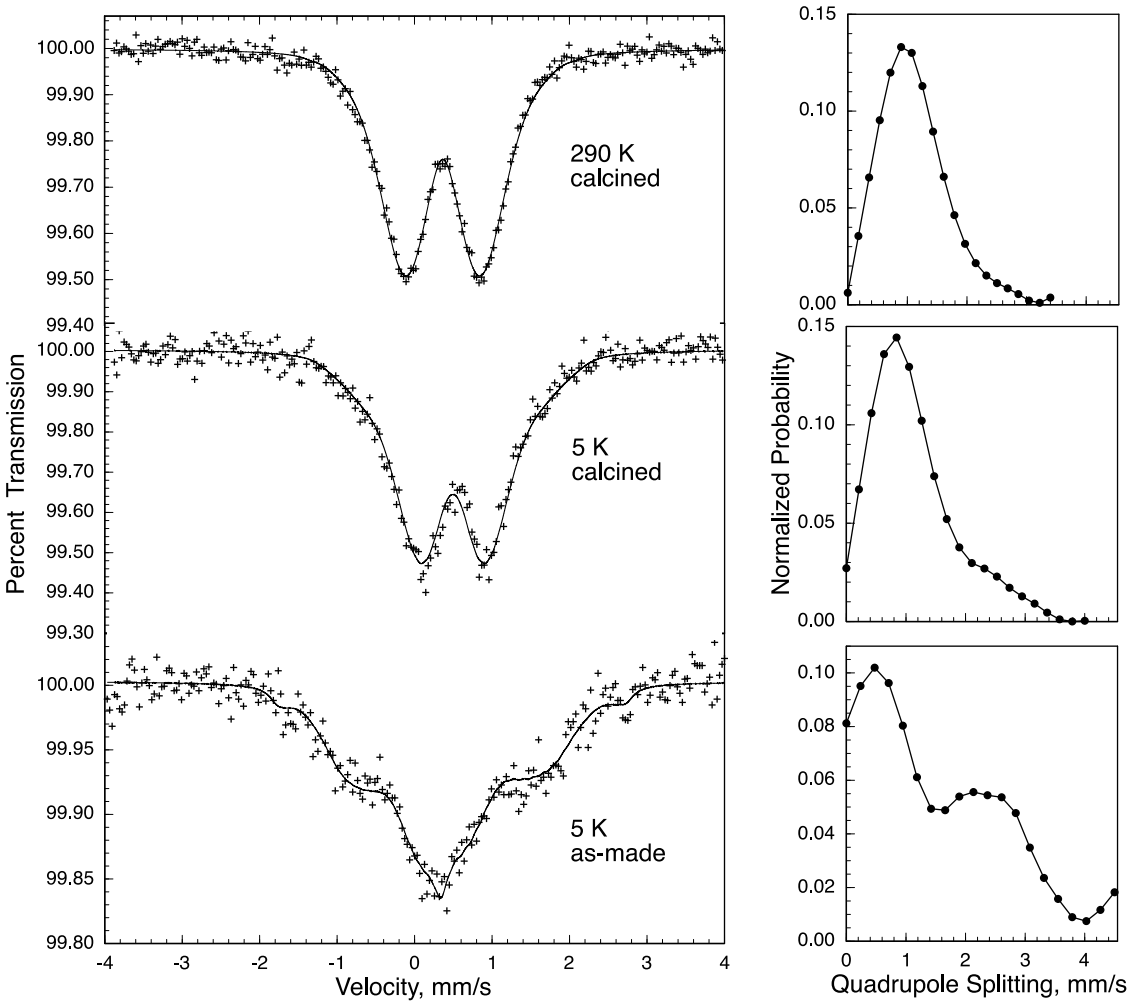

Figure 5. Mössbauer spectra, left, of the calcined and as-made Fe-SSZ-70 zeolite fit with a distribution of quadrupole splittings, right, by using the Le Caër and Dubois method.[44]

of MCM-56 after calcination.[40] However, the broader peak centered at 8.8° remains, which shows that the structure retains the ±1/3 shift. These results are again consistent with those of the previous SSZ-70 synthesis and structure studies.[7,17−19,39]

3.3. Scanning Electron Microscopy. Figure 4 shows SEM images of as-made Fe-SSZ-70 and Al-SSZ-70. The crystals are roughly 0.5−1 μm in diameter and exhibit the typical plate-like morphology of a layered material, which is similar to previously reported SSZ-70 materials.[39] SEM does not show significant differences before and after calcination (Figure S3). Although local rearrangement of some framework atoms typically occurs upon calcination, the apparent crystal morphology remains the same.

3.4. Chemical and Textural Properties. Table 4 shows chemical and textural properties of Fe-SSZ-70 and Al-SSZ-70. Both gels start with an atomic Si/M molar ratio of 50, where M is Fe or Al, and the Si/M ratios in the as-made Fe- and Al-SSZ-70 products are 44 and 40, respectively. Both as-made products seem to incorporate similar amounts of heteroatoms (Fe or Al) during crystallization. After calcination, the Si/M ratios are not significantly changed.

ICP-AES is a bulk measurement technique, however, and it does not differentiate between framework and extra-framework M. TPD using isopropylamine better probes Brønsted acidity and can be used to estimate the M density in the zeolite framework. These experimental values can be compared to a theoretical acid site density in which each M ion is assumed to associate with one acid site; the theoretical values are calculated based on the calcined Si/M ratios obtained from ICP-AES. The experimental acid site density of calcined Fe-SSZ-70 is just over 50% of the theoretical acid site density, which suggests that half the Fe^{3+} is extra-framework. In comparison, 75% of the Al^{3+} in Al-SSZ-70 is associated with an acid site.

Kofke et al. proposed that isopropylamine during TPD experiments only adsorbs onto framework Fe^{3+}.[42] To further support this hypothesis, calcined Fe-SSZ-70 was subjected to 100% steam at 800 °C for 1 h at atmospheric pressure. Under these harsh conditions, all of the Fe^{3+} should be removed from the framework.[43] Indeed, isopropylamine TPD experiments measured zero acid sites, thus showing that the contributions to the acid site density measurements do not come from extra-framework Fe^{3+}.

The micropore volumes of Fe-SSZ-70 and Al-SSZ-70 are both 0.17 cm^3/g and are similar to previously reported values.[39] Furthermore, like other layered materials, the Fe-SSZ-70 crystals exhibit relatively high external surface areas. The Fe^{3+} does not appear to affect the micropore size or surface

https://doi.org/10.1021/acscatal.2c01361
ACS Catal. 2022, 12, 6464−6477

Table 5. Distribution Fit Mössbauer Spectral Parameters[a]

sample	T (K)	δ_o (mm/s)[b]	m[c]	$\langle \Delta E_Q \rangle$ (mm/s)	σ (mm/s)[d]	ΔE_Q fit range (mm/s)
Fe-SSZ-70$_{calcined}$	290	0.366(4)	0.000(5)	1.12(3)	0.58(3)	0.0−3.4
Fe-SSZ-70$_{calcined}$	5	0.494(5)	0.000(5)	1.12(2)	0.71(2)	0.0−4.0
Fe-SSZ-70$_{as\text{-}made}$	5	0.34(2)	0.030(5)	1.50(5)	1.16(5)	0.0−4.5

[a]The statistical errors are given in parentheses. The fits have been obtained by using the Le Caër and Dubois method[44] with the linewidth of each of the 20 components used in the fit constrained to 0.24 mm/s. [b]The isomer shift values are given relative to the α-iron foil measured at 290 K. [c]The linear correlation coefficient, m, is the unitless slope in $\delta_i = \delta_o + m(\Delta E_{Q,i})$. [d]The standard deviation of the weighted average $\langle \Delta E_Q \rangle$ values found in the distribution fits.

area of SSZ-70 when compared to reported values for Si-, Al-, or B-SSZ-70.

3.5. Characterization of the Coordination Environment of Fe^{3+}. To understand the catalytic behavior of Fe-SSZ-70, we must first have a solid understanding of the state of the Fe^{3+}. Is it in the zeolite framework? Does it have a tetrahedral or octahedral environment? What effect does calcination have on the Fe^{3+}? We used Mössbauer spectroscopy, EPR, and DRUV−vis to further probe the Fe^{3+} in as-made and calcined Fe-SSZ-70.

3.5.1. Mössbauer Spectroscopy. The zero-field iron-57 Mössbauer spectra of calcined Fe-SSZ-70 were measured at 290 and 5 K, and the spectrum of as-made Fe-SSZ-70 was measured at 5 K; the experimental spectra are shown as the plus symbols in Figures 5 and S4 and the corresponding fit parameters are given in Table 5.

Initially, the observed Mössbauer spectra were fit with two symmetric quadrupole doublets with a Lorentzian lineshape and the same isomer shifts and line widths; the corresponding spectral fits are shown as the lines in Figure S4; and the corresponding initial fit parameters are given in Table S2. In these initial fits, as-made Fe-SSZ-70 exhibits an isomer shift, δ, of 0.33(2) mm/s at 5 K, whereas calcined Fe-SSZ-70 exhibits a δ of 0.366(4) mm/s at 290 K, a value that increases to 0.493(5) mm/s at 5 K. Any attempt to use two different isomer shifts for the doublets in a given spectrum either failed or refined to virtually the same value.

All of the initial spectral fit parameters for the 5 K as-made Fe-SSZ-70 spectrum are consistent with high-spin Fe^{3+} ions in a predominately four-coordinate pseudo-tetrahedral coordination environment.[37,45] In contrast, all of the initial spectral fit parameters and the changes between 290 and 5 K for the calcined Fe-SSZ-70 spectra are fully consistent with high-spin Fe^{3+} ions in a predominately six-coordinate pseudo-octahedral coordination environment. Indeed, calcining the as-made Fe-SSZ-70 sample has a substantial influence on the local Fe^{3+} coordination environments, with a shift from a four-coordinate pseudo-tetrahedral environment to a predominantly pseudo-octahedral environment. However, the line widths, Γ, of the initial fits are very large, ranging from 0.56 to 1.14 mm/s, which indicate a large distribution in the Fe^{3+} coordination environments, especially in the as-made Fe-SSZ-70.

Because of the very large line widths of the initial Lorentzian fits, as noted above, it is more realistic that all three of the spectra be fit by using the Le Caër and Dubois method[44] with a distribution of 20 quadrupole splittings, $\Delta E_{Q,i}$, a distribution that may or may not show a linear correlation, $\delta_i = \delta_0 + m(\Delta E_{Q,i})$, between the isomer shifts and the quadrupole splittings. Indeed, the three spectra are excellently fit with a distribution consisting of 20 symmetric Lorentzian doublets (see Figure 5 and Table 5). The fits of the 5 and 290 K spectra of the calcined Fe-SSZ-70 sample reveal no observable linear correlation between $\Delta E_{Q,i}$ and δ_i, i.e., m = 0.000(5). In contrast, for the as-made Fe-SSZ-70 sample, there is a small, albeit weak, linear correlation between these two parameters with m = 0.030(5).

As was observed in the initial Mössbauer spectral fits, the distribution fits at 5 K yield an isomer shift of δ_0 = 0.34(2) mm/s for the as-made Fe-SSZ-70 spectrum as compared with a substantially larger δ_0 = 0.494(5) mm/s for the calcined Fe-SSZ-70 spectrum. This increase in the isomer shift is fully consistent with an increase in the Fe^{3+} coordination number from a four-fold pseudo-tetrahedral coordination to a six-fold pseudo-octahedral coordination upon calcination.

3.5.2. Electron Paramagnetic Resonance. For as-made Fe-SSZ-70, the EPR X-band spectrum (Figure 6) acquired at 77 K

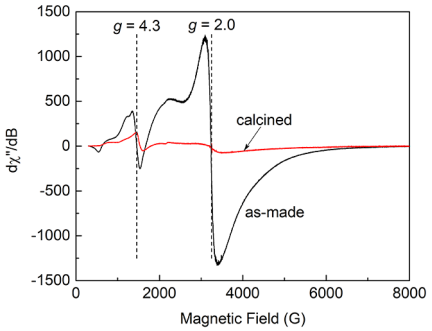

Figure 6. EPR spectra of as-made and calcined Fe-SSZ-70.

shows Fe^{3+} signals with characteristic g-values of 4.3 and 2.0. The g = 2.0 resonance is broad and intense and is assigned to Fe^{3+} in tetrahedral framework positions with relatively high symmetry.[46] The g = 4.3 resonance has been assigned to both framework and extra-framework Fe^{3+}. However, because octahedral sites do not appear until after calcination, the g = 4.3 resonance is assigned to tetrahedral framework Fe^{3+} in more distorted symmetry environments[46] than those that give rise to the g = 2.0 resonance. This assignment is consistent with the distribution fit of the Mössbauer spectral quadrupole splitting (see the lower right portion of Figure 5), which shows a significant contribution of quadrupole splittings greater than 1 mm/s. Additional features of the EPR spectrum include a broad shoulder at low fields below g = 4.3 and an unresolved signal at $g \sim 2.6$. All of the spectral features observed in as-made Fe-SSZ-70 are characteristic of tetrahedral framework Fe^{3+} and are similar to spectra observed in other Fe^{3+}-doped zeolites, such as Fe-**MFI**.[47]

After calcination, the g = 2.0 line decreases in intensity, showing that some Fe^{3+} is released from the framework, resulting in extra-framework Fe^{3+}. However, a small signal at g = 2.0 remains, indicating that calcination does not completely extract all of the Fe^{3+} from the framework. This result is

https://doi.org/10.1021/acscatal.2c01361
ACS Catal. 2022, 12, 6464−6477

consistent with the acid site density measurements on calcined Fe-SSZ-70 that show active adsorption sites and the Mössbauer spectral results discussed above.

3.5.3. Diffuse Reflectance UV−Vis Spectroscopy. Figure 7 shows the DRUV−vis spectra of as-made and calcined Fe-SSZ-70. The as-made Fe-SSZ-70 exhibits a double-band pseudo-absorbance below 300 nm. These two bands centered at 220 and 245 nm are generally associated with O → Fe^{3+} charge-transfer transitions involving isolated tetrahedral Fe^{3+} in zeolitic frameworks. Specifically, the two bands can be assigned to $t_1 \rightarrow t_2$ and $t_1 \rightarrow e$ transitions from a nonbonding orbital (localized on oxygen) to antibonding orbitals (localized on isolated framework Fe^{3+}).[48] In contrast, a pseudo-absorbance band above 300 nm is generally assigned to extra-framework Fe^{3+} centers that are likely present as aggregates (e.g., Fe−O−Fe or even bulk Fe_2O_3).[49] Such a pseudo-absorbance above 300 nm is not observed in as-made Fe-SSZ-70, indicating that Fe^{3+} is present as tetrahedrally coordinated isolated centers in the framework of as-made Fe-SSZ-70. In contrast, the pseudo-absorbance above 300 nm appears after calcination of Fe-SSZ-70, indicating the presence of Fe^{3+} oxide aggregates. This observation suggests that some framework Fe^{3+} centers in as-made Fe-SSZ-70 are removed from the framework upon calcination, forming Fe^{3+} oxide aggregates.

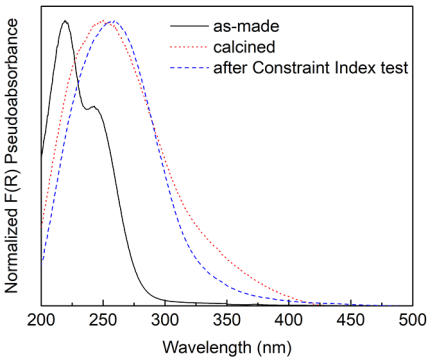

Figure 7. DRUV−vis spectra of as-made and calcined Fe-SSZ-70.

It should be noted that the conclusions drawn from DRUV−vis spectroscopy as a stand-alone technique for determining the coordination environment of Fe^{3+} in zeolites must be interpreted with caution.[48,49] For example, DRUV−vis cannot easily discern between small Fe−O−Fe aggregates and bulk Fe_2O_3. However, the combination of this technique with more conclusive experimental methods applied to Fe^{3+}-containing zeolites can provide useful information.[50,51] In particular, the Mössbauer spectral results described above for calcined Fe-SSZ-70 detect neither a magnetic sextet nor the inner lines of a sextet at 290 and 5 K; if present, such a sextet would indicate the presence of bulk Fe_2O_3. Even bulk, small superparamagnetic Fe_2O_3 particles would be expected to yield a sextet pattern at 5 K. Thus, any extra-framework species present upon calcination exist as pseudo-octahedrally coordinated Fe^{3+} ions that are either isolated species or superparamagnetic aggregates with only a few Fe^{3+} ions.

3.6. Catalytic Testing. The Constraint Index (CI) test was designed to investigate shape selectivity and relative pore sizes in different zeolites.[52,53] These properties are quantified by measuring the ratio of the rates of conversion of *n*-hexane to 3-methylpentane in the acid-catalyzed cracking of an equimolar mixture feed of these two components. Generally, CI values of one or less are typical of large-pore zeolites, while small-pore zeolites have a CI greater than 10. Large cavities within the structure, however, must be accounted for when analyzing the results,[53] as will be discussed below in relation to the *i*C4/*n*C4 ratio in the product. Table 6 gives the CI results after 15 min of time on-stream where we assume that the catalyst is in the "coke-free" state. The conversions of *n*-hexane and 3-methylpentane and their total conversion for Fe-SSZ-70 are all much lower than those of Al-SSZ-70, which suggests that the acid sites associated with framework Fe^{3+} are weaker than the acid sites associated with framework Al^{3+}. This result is also evidenced by the high reaction temperature of 482 °C for Fe-SSZ-70 versus 454 °C for Al-SSZ-70. The CI values are essentially the same for both samples, indicating that the differences in catalytic activity are not due to any differences in the framework structure. The low CI value of about 1 for both samples illustrates the dominance of the larger 12-MR cups over the 10-MR pores in the SSZ-70 structure. The iC_4/nC_4 ratio can provide insight into the internal space that is available for transition states from bimolecular cracking reactions. The iC_4/nC_4 ratio of 0.3 for the Fe-SSZ-70-catalyzed reaction may result because at the very high temperature of 482 °C, the reactivities of *n*-hexane and 3-methylpentane, as well as their intermediates, do not differ significantly. However, the reactivities of the feeds and their intermediates are more sensitive to the strong acid sites of the more active Al-SSZ-70; hence, the Al-SSZ-70-catalyzed reaction shows a much higher iC_4/nC_4 ratio.

Fe-SSZ-70 and Al-SSZ-70 loaded with 0.5 wt % Pd were also tested for the hydrocracking−hydroisomerization of *n*-decane (nC_{10}). In this test, the zeolites are evaluated for their selectivity between cracking and isomerization as the temperature and conversion increase. Figure 8a,b shows the conversion or yield versus temperature for nC_{10} tests for Pd/Fe-SSZ-70 and Pd/Al-SSZ-70, respectively. Conversion of nC_{10} over Pd/Fe-SSZ-70 reaches a maximum of 85% at 371 °C (which was the highest reaction temperature applied in this study) with a total isomerization yield of 74%. Moreover, 64% of the isomerization yield consisted of monobranched isomers, indicating mostly single isomerization events. In contrast, even though Pd/Al-SSZ-70 is more active (i.e., leading to a higher conversion at a lower temperature), it only reaches a maximum of 48% total isomerization yield at 271 °C; 41% of the isomerization yield is monobranched isomers. It is also noteworthy that cracking dominates with Pd/Al-SSZ-70 at higher temperatures. Consistently, Al-SSZ-70 has a higher activity in both CI and nC_{10} hydroconversion.

Table 6. Constraint Index Test Results for Fe-SSZ-70 and Al-SSZ-70

sample	temperature (°C)	*n*-hexane conversion (%)	3-methylpentane conversion (%)	total feed conversion (%)	constraint Index	iC_4/nC_4
Fe-SSZ-70	482	8.9	8.4	8.6	1.1	0.3
Al-SSZ-70	454	74	73	74	1.0	3.8

https://doi.org/10.1021/acscatal.2c01361
ACS Catal. 2022, 12, 6464−6477

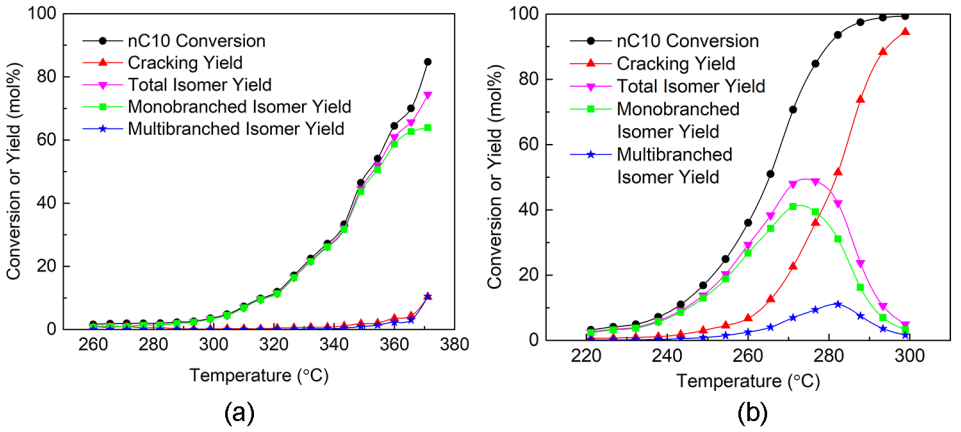

Figure 8. Conversion or yield versus temperature for the hydroconversion of nC_{10} for (a) Pd/Fe-SSZ-70 and (b) Pd/Al-SSZ-70.

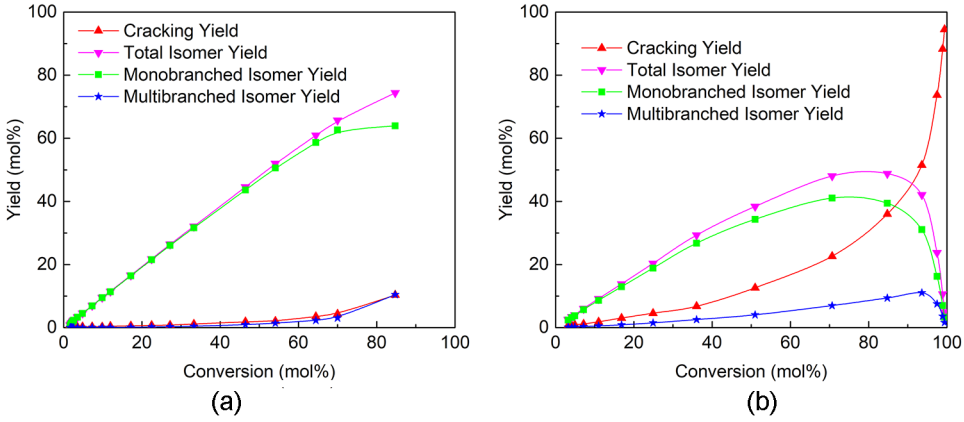

Figure 9. Product yield versus nC_{10} conversion for (a) Pd/Fe-SSZ-70 and (b) Pd/Al-SSZ-70.

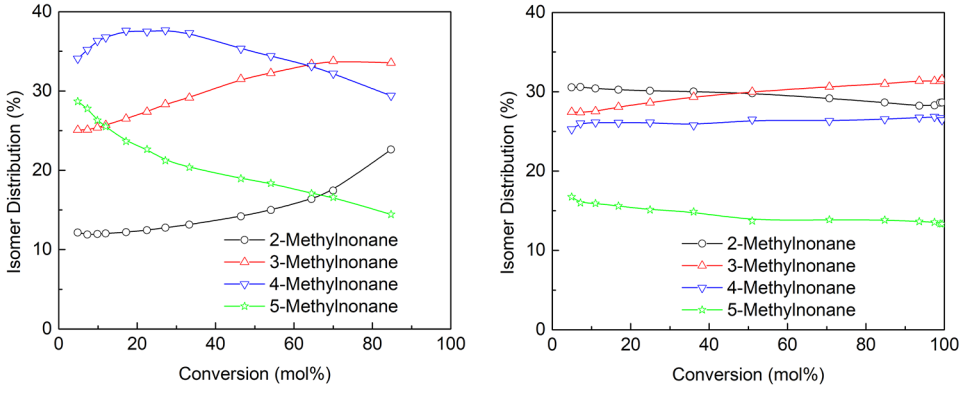

Figure 10. iC_{10} product distribution versus nC_{10} conversion for (a) Pd/Fe-SSZ-70 and (b) Pd/Al-SSZ-70.

(We note that nearly all of the monobranched isomers were methylnonane. Strictly speaking, monobranched isomers can also include 3-ethyloctane, 4-ethyloctane, 4-propylheptane, and 4-isopropylheptane. However, we either saw an insignificant amount or none of these compounds in the GC chromatograms.)

Figure 9a,b replots the data shown in Figure 8 as yield versus conversion curves for Pd/Fe-SSZ-70 and Pd/Al-SSZ-70, respectively. The results for the Pd/Fe-SSZ-70-catalyzed test similarly show that most of the products are monobranched isomers. Even at a conversion of 85%, the cracking yield is only 10%. On the other hand, the Pd/Al-SSZ-70-catalyzed test reaches a maximum total isomer yield of 49% at 85% conversion and exhibited a cracking yield of 36%; cracking yield rapidly increases at higher conversions.

The distribution of C_{10} isomers is shown in Figure 10. At low conversions, Pd/Fe-SSZ-70 results in higher 4- and 5-methylnonane selectivity. These selectivities decrease as conversion increases, and the relative amounts of 2- and 3-methylnonane increase. In contrast, the isomer distribution remains relatively constant for Pd/Al-SSZ-70. Claude and Martens used a combination of experiments and molecular modeling to study monobranching of *n*-alkanes on ZSM-22 and found that the isomer distribution can be explained by two

https://doi.org/10.1021/acscatal.2c01361
ACS Catal. 2022, 12, 6464−6477

types of adsorption: pore mouth and key lock.[54] In pore-mouth mode, one end of the hydrocarbon adsorbs into the mouth of the zeolite pore and thus favors branching at the end of the alkane chain. Central branching of the hydrocarbon occurs during key lock mode, in which the two ends of the alkane adsorb into different pores. In both cases, isomerization occurs at or near the external surface of the zeolite. If such a mechanism is used to explain the results shown in Figure 10, Pd/Fe-SSZ-70 shows key lock mode adsorption at low conversions and trends toward pore-mouth adsorption at higher conversions. In contrast, Pd/Al-SSZ-70 exhibits pore-mouth adsorption throughout the entire conversion range.

To further evaluate the catalyst, the Pd dispersions of Pd/Fe-SSZ-70 and Pd/Al-SSZ-70 samples were measured by H_2 chemisorption (Table 7). The strong dispersions associated with chemisorbed H_2 were 31.1 and 9.9% for Pd/Fe-SSZ-70 and Pd/Al-SSZ-70, respectively. (Weak dispersion is associated with physisorbed H_2, and the combined dispersion is the sum of the strong and weak dispersions.) Although the target Pd loading was 0.5 wt %, the actual Pd loading from ICP-AES shows that the Fe-SSZ-70 has 44% more Pd than Al-SSZ-70. Moreover, the atomic Pd/M ratio was 42% higher for Fe-SSZ-70 than Al-SSZ-70. This may explain why the dispersion for Al-SSZ-70 was lower than Fe-SSZ-70. Furthermore, Song et al. found that extra-framework Fe^{3+} contributed to better Pt dispersion in KL zeolite by adjusting the electronic states of the Pt.[55] Although the noble metal is different in our Fe-SSZ-70 system, it is possible that extra-framework Fe^{3+} may also be a contributing factor to our Pd dispersion. Baseline H_2 chemisorption measurements on the calcined samples (i.e., before Pd-exchange) were also carried out to ensure that neither the Fe nor Al contributes to H_2 chemisorption. The values of −4.1 and −0.9% for Fe-SSZ-70 and Al-SSZ-70, respectively, are relatively low and can be attributed to analytical sensitivity and accuracy of the measurement; hence, H_2 chemisorption is from the Pd alone.

Table 7. Chemical and Pd Dispersion Properties of Calcined and Pd-Loaded Fe-SSZ-70 and Al-SSZ-70

			metal dispersion		
sample	Pd/M[a]	Pd content (wt %)[a]	strong (%)	weak (%)	combined (total; %)
$Fe\text{-}SSZ\text{-}70_{calcined}$			−4.1	−0.3	−4.4
$Pd/Fe\text{-}SSZ\text{-}70_{calcined}$	0.17	0.65	31.1	38.3	69.4
$Al\text{-}SSZ\text{-}70_{calcined}$			−0.9	−0.9	−1.8
$Pd/Al\text{-}SSZ\text{-}70_{calcined}$	0.12	0.45	9.9	22.6	32.5

[a]M = Fe or Al; Pd/M ratios are calculated from Pd, Al, and Fe wt % measurements from ICP-AES.

4. DISCUSSION

4.1. Coordination Environment of Fe^{3+}. Numerous research groups have directly synthesized and tested Fe^{3+}-containing MCM-22,[34,56−60] and Fe^{3+}-containing MCM-56[61] and SSZ-70[35] have been made through post-synthetic treatments. The former groups that incorporated Fe^{3+} into the MCM-22 framework during the synthesis showed that Fe^{3+} was in the framework in the as-made materials. Most studies saw evidence of partial removal of the Fe^{3+} from the framework upon calcination (Wu et al. did not clearly comment on the Fe^{3+} after calcination).

In this study, the Mössbauer, EPR, and DRUV−vis spectroscopy results all converge to the same general conclusion as the studies referenced in the previous paragraph: the Fe^{3+} is tetrahedrally coordinated in the zeolite framework of the as-made materials and some of the Fe^{3+} become octahedrally coordinated after calcination and are removed from the framework. Qualitatively, this result is visible in Figure 11. The as-made sample is a white powder, whereas the calcined powder has a slight orange hue, which is typical of extra-framework Fe_2O_3. Nonetheless, some of the Fe^{3+} does remain in the framework after calcination, and this Fe^{3+} is important for catalytic purposes. Several different calcination protocols (e.g., varying temperature, gas environment, and ozone treatments) were attempted to keep more of the Fe^{3+} in the framework, but none were ultimately successful. Interestingly, other studies on Fe-**MWW** have shown that higher calcination temperatures may result in better catalytic activity for certain applications.[58]

Together with elemental analysis, TPD measurements provide another method to indirectly probe the nature of the

(a) (b)

Figure 11. Photographs of (a) as-made Fe-SSZ-70 and (b) calcined Fe-SSZ-70.

https://doi.org/10.1021/acscatal.2c01361
ACS Catal. 2022, 12, 6464−6477

Fe^{3+} after calcination; the results in Table 4 support the conclusions stemming from the three spectroscopic methods discussed above. The classical picture of Brønsted acid sites in zeolites assumes that each framework heteroatom (Fe or Al) is associated with one Brønsted acid site that results from a proton attached to the bridging oxygen between Si−O−M, while the positively charged proton balances the negative charge on the framework from the M^{3+} ion. Under this assumption, the acid site density results suggest that half of the Fe^{3+} becomes extra-framework after calcination of Fe-SSZ-70 because of the loss of acid sites associated with the presence of extra-framework Fe^{3+}. In contrast, most of the Al^{3+} remains in the framework after calcination of Al-SSZ-70.

These results lead to the question of why all of the Fe^{3+} is difficult to keep in the framework after calcination. There are numerous examples in the literature of other Fe^{3+}-containing zeolite frameworks that can retain the Fe^{3+} to varying extents after calcination. Pérez-Ramírez et al. studied as-made, calcined, and steamed forms of Fe-beta and Fe-ZSM-5 and found that extraction of the Fe^{3+} depends on the zeolite framework.[49] Lázár et al. determined that Fe^{3+} was more stable in framework positions in the ZSM-5 structure than in MCM-22.[62] One explanation is that some crystallographic site locations of the Fe^{3+} in certain frameworks come under more strain than others. Although the specific location of Fe^{3+} has been studied in other zeolite frameworks,[63] to the best of our knowledge, there are no Fe^{3+} siting studies in SSZ-70 or any other members of the **MWW** family. Grosso-Giordano et al. post-synthetically grafted Fe^{3+} onto DZ-1, a delaminated form of SSZ-70, and found that the Fe^{3+} was located on the external surface of the layers.[35] Berkson et al. studied Al^{3+} siting in SSZ-70 and found that 94% of the Al^{3+} is located at the surfaces of the large pores of the layers.[8] The CI value of 1.1 for Fe-SSZ-70 (Table 6) is what would be expected for a large-pore zeolite, which suggests that at least some of the Fe^{3+} in Fe-SSZ-70 is located in the large pores. However, without knowing the precise location of the Fe^{3+} in the SSZ-70 structure, any relationship between framework strain and the stability of the Fe^{3+} during calcination is mostly speculative.

Another DRUV−vis spectrum was measured on the recovered Fe-SSZ-70 sample after the CI test to evaluate any changes to the Fe^{3+} during a catalytic test (Figure 7). The broad shape of the spectrum after the CI test is consistent with that of calcined Fe-SSZ-70, which was obtained before the CI test. There is a slight red shift after the CI test between 200 and 300 nm, which suggests that some of the remaining framework Fe^{3+} may have been removed. Isopropylamine TPD measurements on the recovered Fe-SSZ-70 reveal an acid site density of 142 μmol/g, which means that 79% of the acid sites are still active after the CI test.

4.2. Catalysis. Catalytic testing results using *n*-decane show that Fe-SSZ-70 preferentially catalyzes isomerization over cracking. Changing the heteroatom from Al to Fe in SSZ-70 leads to a discussion about the effects of (1) heteroatom type and (2) the size of the pore systems in SSZ-70 (medium versus large pores). The literature is full of examples showing that these two physicochemical properties greatly contribute to the catalytic performance of zeolites.

The results of the present Fe-SSZ-70 study show that changing the heteroatom, and hence, the acid strength, produces a material with isomerization selectivity approaching that of a 1D, 10-MR.[64] Indeed, previous reports on Fe^{3+}-substituted 1D, 10-MR zeolites, ZSM-22 and ZSM-23, showed that they had better alkane isomer selectivity than their Al^{3+}-containing counterparts.[65−67] The authors of these Fe-ZSM-22 and Fe-ZSM-23 studies generally attributed the better performance to the weaker acidity of Fe over Al. Previous studies in the literature on hydrocracking and hydroisomerization have also found that catalysts with weaker Brønsted acid sites result in more isomerization.[1,68−71] Such results, however, should be analyzed carefully. Noh et al. found that the intrinsic acid site strength is difficult to decouple from diffusional and constraint effects that result from proton reactivity, the zeolite framework topology, crystal size, and acid site density.[72] They studied **MFI** zeolite with Al, Ga, Fe, and B by using a combination of *n*-heptane tests and DFT, and they concluded that secondary reactions that occur within the zeolite channels may hide the true primary selectivity of an acid site between β-scission and isomerization. The intrinsic mechanism of previously reported results in which stronger acids exhibit more β-scission is hidden by the diffusional constraints imposed upon the various transition states by the stronger acids. Although the zeolite topology and crystal sizes of Fe-SSZ-70 and Al-SSZ-70 are the same, diffusional effects are more pronounced in medium-pore zeolites (those with 10-MR) than large-pore zeolites (those with 12-MR).[72,73] SSZ-70 contains 10-MR, 12-MR, and a partially blocked 14-MR, and thus, a more rigorous mechanistic study is required to understand the confluence of acid site strength and pore size on the performances of this SSZ-70 system. Nonetheless, the *gross* result of changing the heteroatom from Al to Fe in this study causes SSZ-70 to become more selective for isomerization.

The catalytic outcomes of this study challenge long-held beliefs that the best isomerization zeolites for producing better-performing fuels and base oils are 1D, 10-MR.[2−4] For the reasons discussed in the introduction, most hydroisomerization studies focus on medium-pore zeolites. Fe^{3+} has been substituted into the frameworks of other large-pore zeolites, but these zeolites have been studied for other applications, such as the selective catalytic reduction of NO_x, methane to methanol, and benzene to phenol.[63] We are unaware of similar studies of Fe^{3+}-containing, 12-MR zeolites that show strong alkane isomerization selectivity.

The unique structure of SSZ-70, combined with the heteroatom type, may help explain the unusual catalytic results. The relatively high external surface area of SSZ-70 and the shallow 12-MR cups may favor isomerization on or near the surface of the zeolite. Layered materials, such as SSZ-70, typically have higher external surface areas than standard zeolites of similar crystal sizes. Zeolites with high external surface area, such as nanozeolites, have been shown to favor pore-mouth catalysis in hydroisomerization.[74] Moreover, the 12-MR side pockets on the surface of the SSZ-70 crystals may be shallow enough for linear alkanes to isomerize to monobranched isomers without forming multibranched or cracked products before diffusing away from the zeolite, a sort of "pseudo-" pore-mouth catalysis. This may be especially true for Fe-SSZ-70, which has high selectivity for monobranched isomers (Figures 8−10). These morphological considerations, combined with the weaker acidity of Fe^{3+}, may explain the high isomerization selectivity of large-pore Fe-SSZ-70. Indeed, Mehla et al. studied a series of large-pore, Al^{3+}-containing, ZSM-12 zeolites and found that those with weaker acidity and higher external surface area favored isomerization over cracking in hydroisomerization reactions using *n*-hexadecane

https://doi.org/10.1021/acscatal.2c01361
ACS Catal. 2022, 12, 6464−6477

as a model feed.[71] However, as noted above by Noh et al., diffusional effects must be dissociated from intrinsic acid strength when studying these zeolites to obtain a true understanding of how Fe affects selectivity between isomerization and cracking.

Finally, as previously discussed, the tetrahedral site locations of the Fe^{3+} in the SSZ-70 framework are unknown. Determination of this information would lead to a better understanding of which pore system in the SSZ-70 framework is catalyzing the reaction. If Fe^{3+} is solely in the 10-MR, then Fe-SSZ-70 could be acting as a 1D, 10-MR. On the other hand, if Fe is in the 12 and/or 14-MR, these catalytic results are certainly unusual for a large-pore zeolite. The low CI value (Table 6) resembles the behavior of a large-pore zeolite and suggests that the location of the Fe is not limited to the 10-MR.

5. CONCLUSIONS

While most studies use 1D, 10-MR zeolites for hydroisomerization, this report shows that heteroatom type (or acid strength), framework, and crystal morphology may also influence product selectivity. Besides being a scientific curiosity, the use of a large-pore zeolite for hydroisomerization may have practical benefits. These materials could be advantageous for feeds with a high wax content, as the larger pores and high external surface areas may be able to better process larger molecules. In addition, other large-pore zeolites may produce similar, or even better, results. Screening a set of other large-pore materials could shed light on what structural or chemical features of this Fe-SSZ-70 system are particularly useful for isomerization. We are continuing to study other Fe-containing zeolites to better understand the confluence of likely intertwined factors, such as pore structure, acid strength, and transport limitations, and we anticipate publishing these results in future papers.

Fe-SSZ-70 was synthesized in both hydroxide and fluoride media using two different SDAs. Mössbauer, EPR, and DRUV−vis spectroscopies all show that Fe^{3+} is tetrahedrally coordinated in as-made Fe-SSZ-70. After calcination, some of the Fe^{3+} is retained in the framework, as evidenced through EPR and DRUV−vis spectroscopies, TPD, and CI and *n*-decane testing. Compared to Al-SSZ-70, Fe-SSZ-70 exhibits surprisingly strong isomerization selectivity, especially for monobranched isomers. These results are particularly notable given that SSZ-70 contains 12-MR and partially blocked 14-MR.

■ ASSOCIATED CONTENT

Supporting Information

The Supporting Information is available free of charge at https://pubs.acs.org/doi/10.1021/acscatal.2c01361.

Additional XRD patterns, SEM images, Pd dispersion measurement conditions, and Quadrupole doublet Mössbauer spectral fits (PDF)

■ AUTHOR INFORMATION

Corresponding Author

Christopher M. Lew − *Chevron Technical Center, Richmond, California 94801, United States;* orcid.org/0000-0003-4568-4461; Email: cmlew@chevron.com

Authors

Cong-Yan Chen − *Chevron Technical Center, Richmond, California 94801, United States*

Gary J. Long − *Missouri University of Science and Technology, University of Missouri, Rolla, Missouri 65409-0010, United States;* orcid.org/0000-0002-6573-5927

Fernande Grandjean − *Missouri University of Science and Technology, University of Missouri, Rolla, Missouri 65409-0010, United States*

Andrew S. Ichimura − *San Francisco State University, San Francisco, California 94132, United States;* orcid.org/0000-0002-7826-102X

Dan Xie − *Chevron Technical Center, Richmond, California 94801, United States;* orcid.org/0000-0003-2467-976X

Nicolás A. Grosso-Giordano − *University of California Berkeley, Berkeley, California 94720, United States;* Present Address: Lilac Solutions, Inc., Oakland, California 94607, United States; orcid.org/0000-0002-0912-366X

Khetpakorn Chakarawet − *University of California Berkeley, Berkeley, California 94720, United States;* Present Address: University of California, Davis, Davis, California 95616 United States.; orcid.org/0000-0001-5905-3578

Howard S. Lacheen − *Chevron Technical Center, Richmond, California 94801, United States*

Kurt O. Jensen − *Chevron Technical Center, Richmond, California 94801, United States*

Abraham Martinez − *University of California Berkeley, Berkeley, California 94720, United States*

Alexander Katz − *University of California Berkeley, Berkeley, California 94720, United States;* orcid.org/0000-0003-3487-7049

Bi-Zeng Zhan − *Chevron Technical Center, Richmond, California 94801, United States*

Stacey I. Zones − *Chevron Technical Center, Richmond, California 94801, United States;* orcid.org/0000-0002-3128-6481

Complete contact information is available at: https://pubs.acs.org/10.1021/acscatal.2c01361

Author Contributions

The manuscript was written through contributions of all authors. All authors have given approval to the final version of the manuscript.

Notes

The authors declare no competing financial interest.

■ ACKNOWLEDGMENTS

The authors thank Kaustav Chaudhuri, Marta Lezcano, Nacira Laiche, and Mark Muraoka for help with obtaining SEM images, Pd dispersion, nitrogen adsorption−desorption, and catalytic testing data, respectively. They thank Duane Hamada for some of the zeolite synthesis work. The authors thank Kaidong Chen and Axel Brait for support of this research.

■ REFERENCES

(1) Park, K.-C.; Ihm, S.-K. Comparison of Pt/zeolite catalysts for *n*-hexadecane hydroisomerization. *Appl. Catal., A* **2000**, *203*, 201−209.
(2) Zhang, M.; Chen, Y.; Wang, L.; Zhang, Q.; Tsang, C.-W.; Liang, C. Shape Selectivity in Hydroisomerization of Hexadecane over Pt Supported on 10-Ring Zeolites: ZSM-22, ZSM-23, ZSM-35, and ZSM48. *Ind. Eng. Chem. Res.* **2016**, *55*, 6069−6078.

(3) Mäki-Arvela, P.; Khel, T. A. K.; Azkaar, M.; Engblom, S.; Murzin, D. Y. Catalytic Hydroisomerization of Long-Chain Hydrocarbons for the Production of Fuels. *Catalysts* **2018**, *8*, 534−560.
(4) Kubů, M.; Millini, R.; Žilkováa, N. 10-ring Zeolites: Synthesis, characterization and catalytic applications. *Catal. Today* **2019**, *324*, 3−14.
(5) Arroyo, J.; Martens, G. G.; Froment, G. F.; Marin, G. B.; Jacobs, P. A.; Martens, J. A. Hydrocracking and isomerization of n-paraffin mixtures and a hydrotreated gasoil on Pt/ZSM-22: confirmation of pore mouth and key−lock catalysis in liquid phase. *Appl. Catal., A* **2000**, *192*, 9−22.
(6) Weitkamp, J.; Jacobs, P. A.; Martens, J. A. Isomerization and Hydrocracking of C_9 Through C_{16} n-Alkanes on Pt/ZSM-5 Zeolite. *Appl. Catal.* **1983**, *8*, 123−141.
(7) Smeets, S.; Berkson, Z. J.; Xie, D.; Zones, S. I.; Wan, W.; Zou, X.; Hsieh, M.-F.; Chmelka, B. F.; McCusker, L. B.; Baerlocher, C. Well-Defined Silanols in the Structure of the Calcined High-Silica Zeolite SSZ-70: New Understanding of a Successful Catalytic Material. *J. Am. Chem. Soc.* **2017**, *139*, 16803−16812.
(8) Berkson, Z. J.; Hsieh, M.-F.; Smeets, S.; Gajan, D.; Lund, A.; Lesage, A.; Xie, D.; Zones, S. I.; McCusker, L. B.; Baerlocher, C.; Chmelka, B. F. Preferential Siting of Aluminum Heteroatoms in the Zeolite Catalyst Al-SSZ-70. *Angew. Chem., Int. Ed.* **2019**, *58*, 6255−6259.
(9) Baerlocher, C.; McCusker, L. B. Database of Zeolite Structures. http://www.iza-structure.org/databases/, accessed May 4, 2020.
(10) Zones, S. I.; Holtermann, D. I.; Innes, R. A.; Pecoraro, A.; Santilli, D. S.; Ziemer, J. N. Zeolite SSZ-25. U.S. Patent 4,826,667. May 2, 1989.
(11) Leonowicz, M. E.; Lawton, J. A.; Lawton, S. L.; Rubin, M. K. MCM-22: A Molecular Sieve with Two Independent Multidimensional Channel Systems. *Science* **1994**, *264*, 1910−1913.
(12) Schroeder, C.; Mück-Lichtenfeld, C.; Xu, L.; Grosso-Giordano, N. A.; Okrut, A.; Chen, C.-Y.; Zones, S. I.; Katz, A.; Hansen, M. R.; Koller, H. A Stable Silanol Triad in the Zeolite Catalyst SSZ-70. *Angew. Chem., Int. Ed.* **2020**, *59*, 10939−10943.
(13) Roth, W. J.; Dorset, D. L. Expanded view of zeolite structures and their variability based on layered nature of 3-D frameworks. *Microporous Mesoporous Mater.* **2011**, *142*, 32−36.
(14) Schreyeck, L.; Caullet, P.; Mougenel, J. C.; Guth, J. L.; Marler, B. PREFER: a new layered (alumino) silicate precursor of FER-type zeolite. *Microporous Mater.* **1996**, *6*, 259−271.
(15) Ikeda, T.; Akiyama, Y.; Oumi, Y.; Kawai, A.; Mizukami, F. The Topotactic Conversion of a Novel Layered Silicate into a New Framework Zeolite. *Angew. Chem., Int. Ed.* **2004**, *43*, 4892−4896.
(16) Dorset, D. L.; Kennedy, G. J. Crystal Structure of MCM-65: An Alternative Linkage of Ferrierite Layers. *J. Phys. Chem. B* **2004**, *108*, 15216−15222.
(17) Zones, S. I.; Burton, A. W. Molecular Sieve SSZ-70 Composition of Matter and Synthesis Thereof. U.S. Patent 7,108,843, September 19, 2006.
(18) Zones, S. I.; Burton, A. W. Hydrocarbon Conversion Using Molecular Sieve SSZ-70. US Patent 7,550,073, June 23, 2009.
(19) Archer, R. H.; Zones, S. I.; Davis, M. E. Imidazolium structure directing agents in zeolite synthesis: Exploring guest/host relationships in the synthesis of SSZ-70. *Microporous Mesoporous Mater.* **2010**, *130*, 255−265.
(20) Ogino, I.; Eilertsen, E. A.; Hwang, S.-J.; Rea, T.; Xie, D.; Ouyang, X.; Zones, S. I.; Katz, A. Heteroatom-Tolerant Delamination of Layered Zeolite Precursor Materials. *Chem. Mater.* **2013**, *25*, 1502−1509.
(21) Grzybek, J.; Kubu, M.; Roth, W. J.; Gil, B.; Čejka, J.; Kasneryk, V. Structural transformation and chemical modifications of the unusual layered zeolite MWW form SSZ-70. *Catal. Today* **2020**, *354*, 133−140.
(22) Runnebaum, R. C.; Ouyang, X.; Edsinga, J. A.; Rea, T.; Arslan, I.; Hwang, S.-J.; Zones, S. I.; Katz, A. Role of Delamination in Zeolite-Catalyzed Aromatic Alkylation: UCB-3 versus 3-D Al-SSZ-70. *ACS Catal.* **2014**, *4*, 2364−2368.
(23) Okrut, A.; Aigner, M.; Schöttle, C.; Grosso-Giordano, N. A.; Hwang, S.-J.; Ouyang, X.; Zones, S. I.; Katz, A. SSZ-70 borosilicate delamination without sonication: effect of framework topology on olefin epoxidation catalysis. *Dalton Trans.* **2018**, *47*, 15082−15090.
(24) Ouyang, X.; Hwang, S.-J.; Xie, D.; Rea, T.; Zones, S. I.; Katz, A. Heteroatom-Substituted Delaminated Zeolites as Solid Lewis Acid Catalysts. *ACS Catal.* **2015**, *5*, 3108−3119.
(25) Zhan, B.-Z.; Zones, S. I.; Lew, C. M. Hydroprocessing of Hydrocarbons Using Delaminated Zeolite Supports as Catalysts. U.S. Patent 9,783,461, August 22, 2017.
(26) Diaz, O. C.; Yarranton, H. W. Applicability of Simulated Distillation for Heavy Oils. *Energy Fuels* **2019**, *33*, 6083−6087.
(27) Jones, A. J.; Carr, R. T.; Zones, S. I.; Iglesia, E. Acid strength and solvation in catalysis by MFI zeolites and effects of the identity, concentration and location of framework heteroatoms. *J. Catal.* **2014**, *312*, 58−68.
(28) Chu, C. T.-W.; Chang, C. D. Isomorphous Substitution in Zeolite Frameworks. 1. Acidity of Surface Hydroxyls in [B]-, [Fe]-, [Ga]-, and [AI]-ZSM-5. *J. Phys. Chem. A* **1985**, *89*, 1569−1571.
(29) Chatterjee, A.; Iwasaki, T.; Ebina, T.; Miyamoto, A. Density functional study for estimating Brønsted acid site strength in isomorphously substituted ZSM-5. *Microporous Mesoporous Mater.* **1998**, *21*, 421−428.
(30) Yuan, S. P.; Wang, J. G.; Li, Y. W.; Jiao, H. Brønsted Acidity of Isomorphously Substituted ZSM-5 by B, Al, Ga, and Fe. Density Functional Investigations. *J. Phys. Chem. A* **2002**, *106*, 8167−8172.
(31) Wang, Y.; Yang, G.; Zhou, D.; Bao, X. Density Functional Theory Study of Chemical Composition Influence on the Acidity of H-MCM-22 Zeolite. *J. Phys. Chem. B* **2004**, *108*, 18228−18233.
(32) Wang, Y.; Zhou, D.; Yang, G.; Miao, S.; Liu, X.; Bao, X. A DFT Study on Isomorphously Substituted MCM-22 Zeolite. *J. Phys. Chem. A* **2004**, *108*, 6730−6734.
(33) Lew, C. M.; Chen, C.-Y.; Zhan, B.-Z.; Zones, S. I. Ferrosilicate SSZ-70 Molecular Sieve, Its Synthesis and Use. U.S. Patent Application 17/241,204, 2021.
(34) Wu, P.; Lin, H.; Komatsu, T.; Yashima, T. Synthesis of ferrisilicate with the MCM-22 structure. *Chem. Commun.* **1997**, *7*, 663−664.
(35) Grosso-Giordano, N. A.; Yeh, A. J.; Okrut, A.; Xiao, D. J.; Grandjean, F.; Long, G. J.; Zones, S. I.; Katz, A. Effect of Defect Site Preorganization on Fe(III) Grafting and Stability: A Comparative Study of Delaminated Zeolite vs Amorphous Silica Supports. *Chem. Mater.* **2017**, *29*, 6480−6492.
(36) Lippens, B. C.; de Boer, J. H. Studies on pore systems in catalysts: V. The *t* method. *J. Catal.* **1965**, *4*, 319−323.
(37) Grandjean, F.; Long, G. J. Best Practices and Protocols in Mössbauer Spectroscopy. *Chem. Mater.* **2021**, *33*, 3878−3904.
(38) Zones, S. I. Synthesis of pentasil zeolites from sodium silicate solutions in the presence of quaternary imidazole compounds. *Zeolites* **1989**, *9*, 458−467.
(39) Archer, R. H.; Carpenter, J. R.; Hwang, S.-J.; Burton, A. W.; Chen, C.-Y.; Zones, S. I.; Davis, M. E. Physicochemical Properties and Catalytic Behavior of the Molecular Sieve SSZ-70. *Chem. Mater.* **2010**, *22*, 2563−2572.
(40) Roth, W. J.; Dorset, D. L.; Kennedy, G. J. Discovery of new MWW family zeolite EMM-10: Identification of EMM-10P as the missing MWW precursor with disordered layers. *Microporous Mesoporous Mater.* **2011**, *142*, 168−177.
(41) Grzybek, J.; Roth, W. J.; Gil, B.; Korzeniowska, A.; Mazur, M.; Čejka, J.; Morris, R. E. A new layered MWW zeolite obtained by direct synthesis with the bifunctional surfactant template and the updated classification of layered zeolite forms obtained by direct synthesis. *J. Mater. Chem. A* **2019**, *7*, 7701−7709.
(42) Kofke, T. J. G.; Gorte, R. J.; Kokotailo, G. T. Stoichiometric Adsorption Complexes in [B]- and [Fe]-ZSM-5 Zeolites. *J. Catal.* **1989**, *116*, 252−262.
(43) Szostak, R.; Nair, V.; Thomas, T. L. Incorporation and Stability of Iron in Molecular-sieve Structures. Ferrisilicate analogues of zeolite ZSM-5. *J. Chem. Soc., Faraday Trans. 1* **1987**, *83*, 487−494.

https://doi.org/10.1021/acscatal.2c01361
ACS Catal. 2022, 12, 6464−6477

(44) Caer, G. L.; Dubois, J. M. Evaluation of hyperfine parameter distributions from overlapped Mössbauer spectra of amorphous alloys. *J. Phys. E: Sci. Instrum.* **1979**, *12*, 1083−1090.
(45) Maier, S. M.; Jentys, A.; Metwalli, E.; Müller-Buschbaum, P.; Lercher, J. A. Determination of the Redox Processes in FeBEA Catalysts in NH_3-SCR Reaction by Mössbauer and X-ray Absorption Spectroscopy. *J. Phys. Chem. Lett.* **2011**, *2*, 950−955.
(46) Lim, J. B.; Cha, S. H.; Hong, S. B. Direct N_2O decomposition over iron-substituted small-pore zeolites with different pore topologies. *Appl. Catal., B* **2019**, *243*, 750−759.
(47) Ferretti, A. M.; Barra, A.-L.; Forni, L.; Oliva, A.; Schweiger, A.; Ponti, A. Electron Paramagnetic Resonance Spectroscopy of Iron-(III)-Doped MFI Zeolite. 1. Multifrequency CW-EPR. *J. Phys. Chem. B* **2004**, *108*, 1999−2005.
(48) Bordiga, S.; Buzzoni, R.; Geobaldo, F.; Lamberti, C.; Giamello, E.; Zecchina, A.; Leofanti, G.; Petrini, G.; Tozzola, G.; Vlaic, G. Structure and Reactivity of Framework and Extraframework Iron in Fe-Silicalite as Investigated by Spectroscopic and Physicochemical Methods. *J. Catal.* **1996**, *158*, 486−501.
(49) Pérez-Ramírez, J.; Groen, J. C.; Brückner, A.; Kumar, M. S.; Bentrup, U.; Debbagh, M. N.; Villaescusa, L. A. Evolution of isomorphously substituted iron zeolites during activation: comparison of Fe-beta and Fe-ZSM-5. *J. Catal.* **2005**, *232*, 318−334.
(50) Zecchina, A.; Rivallan, M.; Berlier, G.; Lamberti, C.; Ricchiardi, G. Structure and nuclearity of active sites in Fe-zeolites: comparison with iron sites in enzymes and homogeneous catalysts. *Phys. Chem. Chem. Phys.* **2007**, *9*, 3483−3499.
(51) Kumar, M. S.; Schwidder, M.; Grünert, W.; Brückner, A. On the nature of different iron sites and their catalytic role in Fe-ZSM-5 DeNOx catalysts: new insights by a combined EPR and UV/VIS spectroscopic approach. *J. Catal.* **2004**, *227*, 384−397.
(52) Frillette, V. J.; Haag, W. O.; Lago, R. M. Catalysis by crystalline aluminosilicates: Characterization of intermediate pore-size zeolites by the "Constraint Index". *J. Catal.* **1981**, *67*, 218−222.
(53) Zones, S. I.; Harris, T. V. The Constraint Index test revisited: anomalies based upon new zeolite structure types. *Microporous Mesoporous Mater.* **2000**, *35-36*, 31−46.
(54) Claude, M. C.; Martens, J. A. Monomethyl-Branching of Long n-Alkanes in the Range from Decane to Tetracosane on Pt/H-ZSM-22 Bifunctional Catalyst. *J. Catal.* **2000**, *190*, 39−48.
(55) Song, J.; Ma, H.; Tian, Z.; Yan, L.; Xu, Z.; Liu, Q.; Qu, W. The effect of Fe on Pt particle states in Pt/KL catalysts. *Appl. Catal., A* **2015**, *492*, 31−37.
(56) Testa, F.; Crea, F.; Diodati, G. D.; Pasqua, L.; Aiello, R.; Terwagne, G.; Lentz, P.; Nagy, J. B. Synthesis and characterization of Fe- and [Fe,Al]-MCM-22 zeolites. *Microporous Mesoporous Mater.* **1999**, *30*, 187−197.
(57) Berlier, G.; Pourny, M.; Bordiga, S.; Spoto, G.; Zecchina, A.; Lamberti, C. Coordination and oxidation changes undergone by iron species in Fe-MCM-22 upon template removal, activation and red−ox treatments: an in situ IR, EXAFS and XANES study. *J. Catal.* **2005**, *229*, 45−54.
(58) Xiao, P.; Wang, Y.; Osuga, R.; Kondo, J. N.; Yokoi, T. One-pot synthesis of highly active Fe-containing MWW zeolite catalyst: Elucidation of Fe species and its impact on catalytic performance. *Adv. Powder Technol.* **2021**, *32*, 1070−1080.
(59) Mihályi, R.; Lázár, K.; Kollár, M.; Lónyi, F.; Pál-Borbély, G.; Szegedia, Á. Structure, acidity and redox properties of MCM-22 ferrisilicate. *Microporous Mesoporous Mater.* **2008**, *110*, 51−63.
(60) Chen, J.; Peng, G.; Zheng, W.; Zhang, W.; Guo, L.; Wu, X. Excellent performance of one-pot synthesized Fe-containing MCM-22 zeolites for the selective catalytic reduction of NO_x with NH_3. *Catal. Sci. Technol.* **2020**, *10*, 6583−6598.
(61) Grzybek, J.; Gil, B.; Roth, W. J.; Skoczek, M.; Kowalczyk, A.; Chmielarz, L. Characterization of Co and Fe-MCM-56 catalysts for NH_3-SCR and N_2O decomposition: An in situ FTIR study. *Spectrochim. Acta, Part A* **2018**, *196*, 281−288.
(62) Lázár, K.; Szegedi, Á.; Martinez, F.; Molina, R.; Fejes, P.Stabilization of iron in micro-and mesoporous ferrisilicates (MFI, MCM-22, SBA-15, and MCM-41) as detected by in situ Mössbauer spectroscopy. In *Studies in Surface Science and Catalysis*, Elsevier, 2005; Vol. *158*, pp 733−740.
(63) Snyder, B. E. R.; Bols, M. L.; Schoonheydt, R. A.; Sels, B. F.; Solomon, E. I. Iron and Copper Active Sites in Zeolites and Their Correlation to Metalloenzymes. *Chem. Rev.* **2018**, *118*, 2718−2768.
(64) Yang, L.; Wang, W.; Song, X.; Bai, X.; Feng, Z.; Liu, T.; Wu, W. The hydroisomerization of *n*-decane over Pd/SAPO-11 bifunctional catalysts: The effects of templates on characteristics and catalytic performances. *Fuel Process. Technol.* **2019**, *190*, 13−20.
(65) Liu, S.; Ren, J.; Zhu, S.; Zhang, H.; Lv, E.; Xu, J.; Li, Y.-W. Synthesis and characterization of the Fe-substituted ZSM-22 zeolite catalyst with high n-dodecane isomerization performance. *J. Catal.* **2015**, *330*, 485−496.
(66) Chen, Y.; Li, C.; Chen, X.; Liu, Y.; Tsang, C.-W.; Liang, C. Synthesis and Characterization of Iron-Substituted ZSM-23 Zeolite Catalysts with Highly Selective Hydroisomerization of n-Hexadecane. *Ind. Eng. Chem. Res.* **2018**, *57*, 13721−13730.
(67) Me'riaudeau, P.; Tuan, V. A.; Hung, L. N.; Nghiem, V. T.; Naccache, C. Characterization of isomorphously substituted ZSM-23 and catalytic properties in *n*-buteneisomerization. *J. Chem. Soc., Faraday Trans.* **1998**, *94*, 467−471.
(68) Corma, A.; Martinez, A.; Pergher, S.; Peratello, S.; Perego, C.; Bellusi, G. Hydrocracking-hydroisomerization of n-decane on amorphous silica-alumina with uniform pore diameter. *Appl. Catal., A* **1997**, *152*, 107−125.
(69) Zhang, W.; Smirniotis, P. G. Effect of Zeolite Structure and Acidity on the Product Selectivity and Reaction Mechanism for *n*-Octane Hydroisomerization and Hydrocracking. *J. Catal.* **1999**, *182*, 400−416.
(70) Bi, Y.; Xia, G.; Huang, W.; Nie, H. Hydroisomerization of long chain *n*-paraffins: the role of the acidity of the zeolite. *RSC Adv.* **2015**, *5*, 99201−99206.
(71) Mehla, S.; Krishnamurthy, K. R.; Viswanathan, B.; John, M.; Niwate, Y.; Kumar, S. A. K.; Pai, S. M.; Newalkar, B. L. n-Hexadecane hydroisomerization over BTMACl/TEABr/MTEABr templated ZSM-12. *Microporous Mesoporous Mater.* **2013**, *177*, 120−126.
(72) Noh, G.; Zones, S. I.; Iglesia, E. Consequences of Acid Strength and Diffusional Constraints for Alkane Isomerization and β-Scission Turnover Rates and Selectivities on Bifunctional Metal-Acid Catalysts. *J. Phys. Chem. C* **2018**, *122*, 25475−25497.
(73) Noh, G.; Shi, Z.; Zones, S. I.; Iglesia, E. Isomerization and β-scission reactions of alkanes on bifunctional metalacid catalysts: Consequences of confinement and diffusional constraints on reactivity and selectivity. *J. Catal.* **2018**, *368*, 389−410.
(74) Zhang, L.; Fu, W.; He, L.; Cai, G.; Chen, Q.; Tang, T. Design and synthesis of Pt catalyst supported on ZSM-22 nanocrystals with increased accessible 10-MR pore mouths and acidic sites for long-chain n-alkane hydroisomerization. *Microporous Mesoporous Mater.* **2021**, *313*, No. 110834.

https://doi.org/10.1021/acscatal.2c01361
ACS Catal. 2022, 12, 6464−6477